The organization of near-wall turbulence: a comparison between boundary layer SPIV data and channel flow DNS data

Sophie Herpin, M. Stanislas, J. Soria

Journal of Turbulence
Vol. 00, No. 00, 2009, 1–28

RESEARCH ARTICLE

The organization of near-wall turbulence: a comparison between boundary layer SPIV data and channel flow DNS data

S. Herpin[ab*] and M. Stanislas[a] and J. Soria[b]

[a] *Laboratoire de Mécanique de Lille, Ecole Centrale de Lille, Bd Paul Langevin, Cité Scientifique, 59655 Villeneuve d'Ascq cedex, FRANCE (LML UMR CNRS 8107)*;
[b] *Laboratory for Turbulence Research in Aerospace and Combustion, Department of Mechanical and Aerospace Engineering, Monash University, VIC 3800, AUSTRALIA*

(*v0.0*)

The vortical structures of near-wall turbulence at moderate Reynolds number are analyzed and compared in datasets obtained from stereoscopic particle image velocimetry (SPIV) in a turbulent boundary layer and from direct numerical simulations (DNS) in a turbulent channel flow. The SPIV data is acquired in the LTRAC water-tunnel at $Re_\tau = \delta^+ = 820$ in a streamwise/wall-normal plane, and in the LML wind-tunnel at $Re_\tau = \delta^+ = 2590$ in a streamwise/wall-normal plane and in a plane orthogonal to the mean flow. The DNS data is taken from DelAlamo et al [1], at $Re_\tau = 950$. The SPIV database is validated through an analysis of its mean velocity profile and power spectra, which are compared to reference profiles. A common detection algorithm is then applied to both the SPIV and DNS datasets in order to retrieve the streamwise and spanwise vortices. The algorithm employed is based on the 2D swirling strength and on a fit of an Oseen vortex model, which allows to retrieve the vortex characteristics, including its radius, vorticity, and position of the center. At all Reynolds numbers, the near-wall region is found to be the most densely populated region, predominantly with streamwise vortices that are on average smaller and more intense than spanwise vortices. In contrast, the logarithmic region is equally constituted of streamwise and spanwise vortices having equivalent characteristics. Two different scalings were employed to analyze the vortex radius and vorticity : the wall-unit scaling and the Kolmogorov scaling. In wall-unit scaling, a good universality in Reynolds numbers of the vortices radius and vorticity is observed in the near-wall and logarithmic region: the vorticity is found to be maximum at the wall, decreasing first rapidly and then slowly with increasing wall-normal distance; the radius is increasing slowly with wall-normal distance in both regions, except for the streamwise vortices for which a sharp increase in radius is observed in the near-wall region. However, the wall-units scaling is found to be deficient in the outer region, where Reynolds number effects are observed. The Kolmogorov scaling appears to be universal both in Reynolds number and wall-normal distance across the three regions investigated, with a mean radius on the order of 8η and a mean vorticity on the order of $1.5\tau^{-1}$, but for the SPIV data only. In the DNS dataset, the radius in Kolmogorov scaling slowly decreases with wall-normal distance. This difference between the SPIV and the DNS may be linked to a difference between the boundary layer flow and the channel flow, rather than to the techniques themselves. Finally, the distribution of the vorticity of the detected vortices seem to follow faithfully a log normal distribution, in good agreement with Kolmogorov's theory ([2]).

Keywords: Coherent structures; Near-wall turbulence; Vortical structures; Particle Image Velocimetry; Direct Numerical Simulation.

*Corresponding author. Email: sophie_herpin@yahoo.fr

ISSN: 1468-5248 (online only)

DOI: 10.1080/14685240YYxxxxxxx
http://www.informaworld.com

1. Introduction

Turbulence is one of the most challenging problem of fluid mechanics, because of its non-linear, multiscale, and three-dimensional nature. Despite this complexity, early studies using flow visualization and hot-wire anemometry ([3]) have shown that turbulent flows present a remarkable degree of organization, with the occurrence of the so-called coherent structures.

These structures are defined by Robinson [4] as *'three-dimensional region[s] of the flow over which at least one fundamental flow variable exhibits significant correlation with itself or with another flow variable over a range of space and/or time that is significantly larger than the smallest local scales of the flow'*. They exist in a wide range of sizes and shapes, including vortical structures, low and high speed streaks, ejection and sweeps, and a range of large scale and very large scale motions.

The study of coherent structures is rather complex, because having a complete view of them would require near-wall turbulence data over a large range of Reynolds number, that would be time-resolved, volumetric, and possessing a large spatial dynamic range (SDR). Although this type of data is still out of reach, the advent of quantitative and full field techniques such as particle image velocimetry (PIV) or Direct numerical simulations (DNS) provide new insight into the organization of wall-bounded turbulence.

The two techniques present specific advantages and constraints:

- PIV data present the advantage of being unequivocally "real" and can be collected over a very large range of Reynolds numbers; on the other hand, it is limited to 2 dimensions (although 3D techniques are in development), and is averaged over the interrogation window. Furthermore, the size of the camera CCD array and the presence of measurement noise (that need to be assessed) impose some limitations on the data spatial dynamic range ([5]).
- DNS data present the advantage of being 3D, noise free, and without averaging over an interrogation spot; on the other hand, they are limited to moderate Reynolds numbers at the moment and still depend on artificially generated initial conditions.

The spatial dynamic range (SDR) achieved in recent PIV and DNS studies were compared in Herpin et al [6] (see table 1). The SDR was defined as the ratio of the field of view over two times the interrogation window size for PIV, and as the size of computational domain, over twice the mesh spacing for the DNS. In any cases, it was shown that the spatial dynamic range of PIV was much smaller than that of DNS, where by definition all the coherent structures *must* be resolved. The study of Herpin et al [6] proposed a new SPIV dataset at $Re_\theta = 2200$ where 4 PCO4000 with large CCD arrays were used, which allowed to achieve a large SDR about three times larger than that of previous PIV studies, and which was roughly half the one required to resolve a full hairpin packet.

The hairpin packet model shown in figure 1 was proposed by the Urbana Champaign group, and is based on the complementary analysis of DNS ([10]) and PIV ([7]) data. Zhou et al [10] computed using DNS at $Re_\tau = 180$ the evolution of a single hairpin vortex placed in an initially unidirectional flow with no fluctuations. They showed that this primary hairpin had the ability to generate secondary structures, provided it had sufficient initial strength with respect to the background flow. Adrian et al [7] used photographic PIV in the XY plane of a turbulent boundary layer at moderate to high Reynolds numbers ($930 < Re_\theta < 6845$) and identified in instantaneous velocity fields groups made of up to ten hairpins, with the group

Reference	Technique (Plane 1-2)	Re_θ	δ^+ Re_τ	Field of View S_1, S_2	$L^+_{IW,1}, L^+_{IW,2}$	SDR_{th} $\frac{S_i^+}{2*IW^+}$
[7]	Ph-PIV	930	355	$1.5\delta, 1.2\delta$	9,9	30
		2370	836	$1.4\delta, 1.3\delta$	20,20	29
		6845	2000	$1.4\delta, 1.4\delta$	36,25	39
[8]	SPIV(y-z)	7500	2500	500^+, 750^+	11,11	23
[9]	DualPIV(x-z)	2800	1160	$1.1\delta, 1.1\delta$	24,24	27
[1]	DNS		934	$8\pi\frac{h}{2}$,$3\pi\frac{h}{2}$	11,6	1068
[6]	SPIV(x-y)	2200	1360	2.6δ, 0.75δ	13.6, 13.6	115

Table 1. Literature survey of the Spatial Dynamic range SDR_{th} of recent PIV studies, adapted from [6] and completed with their SPIV experiment at $Re_\theta = 2200$

members having small dispersion in their convection velocity, and being spaced several hundreds of wall units apart in the streamwise direction. The packets typically had a streamwise extent of 1.3δ, and made an angle of 12°.

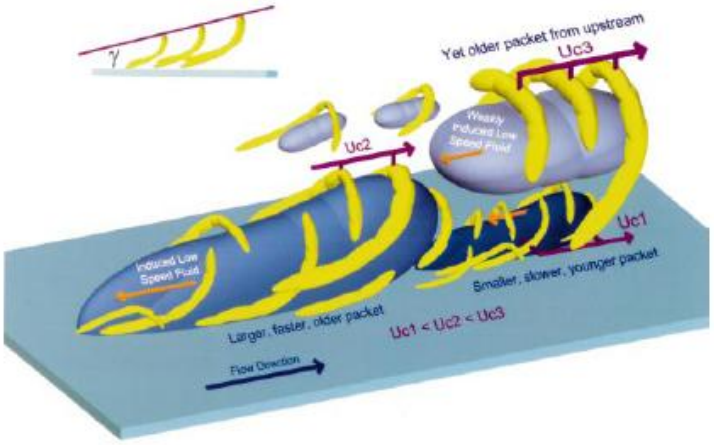

Figure 1. The hairpin packet model, from [7]

With the continuous progress of numerical simulations, measurement techniques, and post-processing tools, more recent studies have provided and continue to provide a more extensive characterization of the structure of near-wall turbulence.

Due to their limited spatial dynamic range, PIV studies have focused their attention either on individual vortices or on the large scale structures, but seldom on both. A number of studies have looked at large-scale structures in XZ planes of turbulent boundary layer: [11] examined the low momentum elongated region of a turbulent boundary layer at $930 < Re_\theta < 6845$ using standard PIV, while [12] looked at hairpin packets using Stereo-PIV in a turbulent boundary layer at $Re_\theta = 2500$; [13] studied the low-speed and the high speed streaks in the buffer layer of a turbulent boundary layer at $Re_\theta = 7800$ measured with SPIV.

On the other hand, several studies have looked at individual vortices. Carlier and Stanislas [8] have investigated cross-section of vortical structures in cross-stream planes inclined at 45° and 135° to the wall, in the range $Re_\theta \in [8000; 19000]$. The wall-normal evolution of the mean characteristics of the detected vortices (radius,

vorticity) were found to be universal in wall-units, with a constant circulation: the radius was found to increase slowly and the vorticity to decrease slowly with increasing wall-normal distance. The population trends of prograde and retrograde spanwise vortices as a function of wall-normal position, Reynolds number (in a range $Re_\tau \in [570; 3450]$) and flow (either boundary layer flow or channel flow) was documented in detail by Wu and Christensen [14] using PIV in a XY plane. The orientation of vortical structures at $y^+ = 110$ and $y/\delta = 0.53$ in a turbulent boundary layer at $Re_\theta = 2500$ was analyzed by Ganapathisubramani et al [9] using dual-plane PIV. A comparison of this SPIV dataset with DNS data at similar Reynolds number was undertaken by Saikrishnan et al [15], with an averaging scheme applied to the DNS. Finally, the scaling of streamwise vortices at $Re_\theta = 7800$ and $Re_\theta = 15000$ was investigated by [16] using stereo-PIV measurements in a plane orthogonal to the mean flow (YZ). The PDF of their radius and intensity were found to be universal both in Reynolds number and in wall-normal distance when scaled with the local Kolmogorov scales η and v. The equation for the mean square vorticity fluctuations was revisited, and a new balance was proposed in the near-wall region.

Direct numerical simulations of turbulent channel flows were performed by Tanahashi et al [17], Das et al [18] and Kang et al [19] in a range of Reynolds number varying from $Re_\tau = 100$ to $Re_\tau = 1270$. For $100 < Re_\tau < 800$, they showed that the probability density functions of the vortices diameter and maximum azimuthal velocity were universal in Re and have a weak dependence in y when non-dimensionalized with the local Kolmogorov scales η and v. Kang et al [19] extended this scaling of the fine scale eddies up to $Re_\tau = 1270$. In addition, clusters of fine-scale eddies and their dynamics were also investigated. The clusters are observed within low-momentum regions of the outer region, and their size increases with increasing wall-normal distance. Using conditional averaging, they showed that the low momentum regions play an important role in the production of the Reynolds shear stress and in the dissipation of turbulent kinetic energy.
The largest range of Reynolds number in DNS of turbulent channel flow have been achieved thanks to a joint effort between Stanford, Madrid and Urbana Champaign universities. The vortex large-scale organization in the logarithmic region of turbulent channel flow was studied by DelAlamo et al [1] in a range of Reynolds number varying from $Re_\tau = 180$ up to $Re_\tau = 1900$. The mean radius and maximum azimuthal velocity were found to depend little of Re_τ and y when scaled with the Kolmogorov lengthscale η and the RMS turbulence intensity. Both tall cluster attached to the wall and small clusters detached from the wall were identified. The scaling of the attached clusters is self-similar such that their dimensions Δ_x, Δ_y and Δ_z are given by $\Delta_x = 3\Delta_y$ and $\Delta_z = 1.5\Delta_y$. The detached clusters are found to scale with the Kolmogorov scales. The attached clusters are parts of larger regions of low-momentum flow whose average geometry is consistent with a cone tangent to the wall along the streamwise axis. It is assumed that the low-momentum region and the clusters are part of a self-sustaining and self-similar process, where the low-momentum region are wakes left behind clusters, while the clusters themselves are triggered by the wakes left by yet larger clusters in front of them.

A number of aspects of the organization of near-wall turbulence remains unclear in the light of these recent results. One difficulty arise from the fact that the qualitative analysis of a few instantaneous velocity fields can provide useful scenarios ([7]), but that these scenarios may not be representative. Another difficulty is linked to the variety of detection schemes used: the results of one study is then sometimes hard to compare with another. In this context, the present study aims at contributing to the current knowledge on the organization of near-wall turbulence

Table 2. Properties of the boundary layer under investigation in the LTRAC water-tunnel

Re_θ	U_∞ (m/s)	Tu ($\%U_\infty$)	δ^+	1^+ (ν/U_τ) (μm)
1300	0.429	2.6%	820	43

at moderate Reynolds number by:

- analyzing statistical results on the streamwise and spanwise vortices, including their scaling laws
- comparing the results obtained from PIV data with those obtained from DNS data

For that purpose, two SPIV datasets are acquired in two complementary flow facilities, and then analyzed and compared with a DNS dataset from [1], which is post-processed using the same detection scheme.

2. SPIV and DNS data of wall-bounded turbulence

2.1. *SPIV data*

The boundary layer data was acquired by means of stereoscopic particle image velocimetry in the LTRAC water-tunnel in Melbourne (Australia) and the LML wind-tunnel in Lille (France), in the range of Reynolds number typically achieved in recent DNS simulations.

In both facilities, the measurements were realized using the same principle : four cameras arranged in two stereoscopic systems with their field-of-view just overlapping: this technique allow to increase the size of the field of view while maintaining a good spatial resolution. The PIV evaluation was performed using the same in-house code 'pivlml' from LML, which features a multipass/multigrid algorithm, a Soloff reconstruction and a misalignment correction. All images were evaluated using a final interrogation window size of $32px * 32px$.

Some details on the specificities of the experimental setup employed in each facility are given below.

2.1.1. LTRAC water-tunnel

An extensive characterization of the facility can be found in Kostas [20]. The measurements were realized in a streamwise/wall-normal (X-Y) plane of a turbulent boundary layer at moderate Reynolds numbers ($Re_\tau = \delta^+ = 820$), with a relatively high free-stream turbulence intensity, on the order of $2.6\%U_\infty$. The specifications of the boundary layer are summarized in table 2.

Extensive details on the experimental procedure and qualification of the data can be found in Herpin et al [6] and Herpin [21]. The measurements were realized using four PCO 4000 cameras arranged in two stereoscopic systems, at a viewing angle of 30° and with the field-of-view just overlapping in the streamwise direction to ensure continuity of the data. The arrangement is shown in Figure 2: it allows to increase the spatial dynamic range in the streamwise direction in order to capture the large scale structures elongated in that direction while maintaining good resolution of the small scales. In order to minimize optical distortions caused by the non-orthogonal viewing through the air-water interface, water-filled prisms with a nominal angle of 30° were placed on each side of the water-tunnel, flush to the walls, in the same fashion as in [22]. The flow was seeded with hollow glass spheres with a mean diameter of $d_p = 11\mu m$. The cameras were fitted with 200mm focal length lenses and an average magnification of $M = 0.45$ was used, corresponding to a spatial

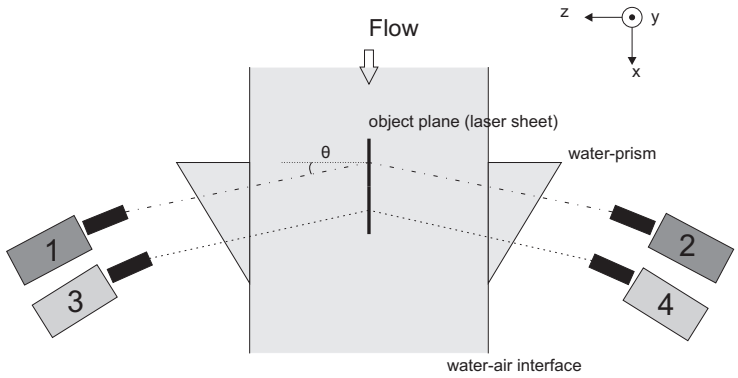

Figure 2. Top-view of the Stereo-PIV setup. Note that the coordinate system is indicative only and does not represent the axes-origin.

resolution of $20.5\mu m/px$ and to a final interrogation window size of 15^+. At the selected aperture ($f_\# = 16$) of the 200 mm focal length lenses, the diffraction limited particle image diameter is on the order of $d_p = 3.4$ px. This value is close to the optimum particle image diameter of 2 px proposed by [23] to reduce peak-locking bias error.

A two-cavity 200 mJ Nd:YAG laser system was used at a wavelength of $\lambda = 532$ nm to illuminate the field of view. With the arrangement employed, the 2 stereo systems had their 2 cameras symmetrically placed on either side of the laser sheet: the field of views of both stereo cameras are then identically stretched, allowing for a more accurate reconstruction of the out-of-plane component. The time delay of the laser illuminating the field of view was chosen to have a maximum displacement on the order of 12 px.

All images were evaluated using the in-house code 'pivlml'. The instantaneous velocity fields from the two stereoscopic systems were merged together by taking the average of the two velocity fields in the overlap region of the fields of view. The data uncertainty was evaluated in the overlap region of the two stereoscopic systems ([6]): it is on the order of 0.75% of U_∞ on the in-plane velocity components, and 1.5% of U_∞ on the out-of plane component. Thanks to the large CCD array of the PCO 4000 camera the data feature a large spatial dynamic range with an interrogation window size of 15^+ and a total field of view of $[S_x; s_y] = [4\delta, 1.4\delta]$.

2.1.2. LML wind-tunnel

The LML wind-tunnel has been extensively described and characterized in Carlier and Stanislas [8] as well as in Carlier [24]. A sketch of the facility is shown in figure 3. The turbulent boundary layer under study develops on the lower wall of the working section after being tripped at the entrance by a grid fixed on the floor. Due to the long length of the working section ($21.6m$ at most), this facility is suitable for high spatial resolution measurements at high Reynolds numbers. The turbulence level in the free-stream is about 0.3% of the external velocity U_∞. The turbulent boundary layer under interest in this contribution is at $Re_\tau = \delta^+ = 2590$, and its characteristics are summarized in table 3.

Table 3. Properties of the boundary layer in the LML wind-tunnel at x=18m obtained from single wire HWA

Re_θ	U_∞ (m/s)	δ^+	δ (m)	1^+ (ν/U_τ) (μm)
7630	3	2590	0.332	128

Extensive details on the experimental procedure can be found in Herpin[21]. The

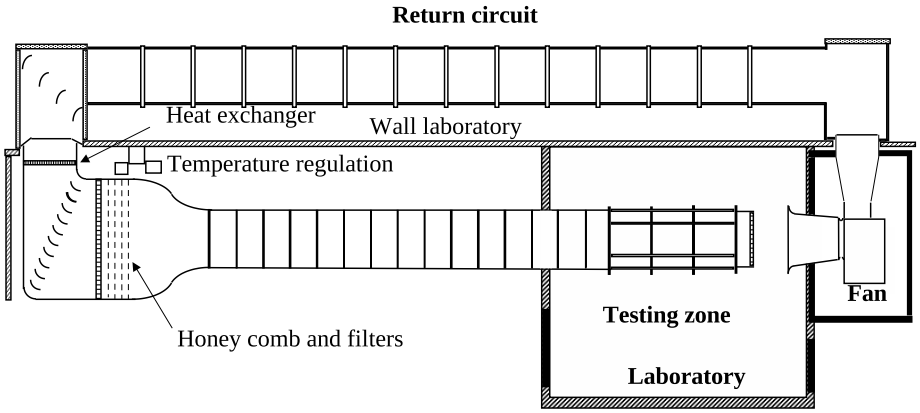

Figure 3. The LML wind-tunnel

datasets at $Re_\tau = \delta^+ = 2590$ were acquired both in a streamwise/wall-normal (XY) plane and in a spanwise/wall-normal (YZ) plane of a turbulent boundary layer in the LML wind-tunnel. The methodology employed is similar to that of the LTRAC water-tunnel, except that the two stereoscopic systems are at a viewing angle of 45° (in order to get a comparable accuracy on the in-plane velocity components and on the out-of-plane velocity component ([25])) and that the systems are overlapping in the wall-normal direction because of the large boundary layer thickness. The camera employed are of type PCO with CCD arrays of $1024 * 1280\ px^2$ and $1376 * 1040\ px^2$, and were fitted with lenses of 105 mm focal length at aperture of $f_\# = 8$. The optical magnification was set to $M = 0.2$, leading to a spatial resolution of $67\mu m/px$, and to a final interrogation window size of 16.8^+.
A two-cavity 200 mJ Nd:YAG laser system was used at a wavelength of $\lambda = 532$ nm to illuminate the field of view with a 1 mm thick laser sheet. The time delay of the laser was also chosen to get a maximum displacement close to 12 px. For the YZ configuration, the mean flow is normal to the measurement plane, creating large out-of-plane motions. In order to keep a high level of cross-correlation, the light sheets from the two illumination pulses were therefore shifted in the out-of-plane direction by a distance corresponding to the mean out-of-plane displacement ([23]). This method reduces the out-of-plane loss of particle pairs while maintaining both a high velocity dynamic range (in contrast to the technique that consist in reducing the separation time) and a high spatial dynamic range (in contrast to the thickening of the laser sheet that induce more spatial averaging). The flow was seeded with tracer particles delivered by a Poly-Ethylene-Glycol smoke generator with a mean particle diameter of $1\mu m$
All images were evaluated using the in-house code 'pivlml'. The instantaneous velocity fields from the two stereoscopic systems were merged together by taking the average of the two velocity fields in the overlap region of the fields of view. In the XY and YZ planes, the measurement feature low uncertainty ($0.7\%U_\infty$ for all velocity components) and high spatial resolution (with an interrogation window size of 16.8^+ and a mesh spacing of 3.9^+).

2.1.3. Summary of the SPIV data

The characteristics of the final data are summarized in table 4. There is a good consistency in interrogation window size ($L_{IW}^+ \approx 16$) and mesh spacing ($\approx 4^+$) for all datasets, and the uncertainties are comprised between $0.7\%U_\infty$ and $1.5\%U_\infty$. The range of Reynolds number achieved is close to that of recent DNS data.

Facility	Plane (1-2)	Re_θ	δ^+ Re_τ	Field of View S_1, S_2	L_{IW}	Mesh spacingΔ_i	1st pt y	n° records
LTRAC	XY	1300	820	4δ, 1.4δ	15.2^+	4.5^+	13^+	605
LML	XY	7630	2590	0.15δ, 0.6δ	16.8^+	3.9^+	24^+	3840
LML	ZY	7630	2590	0.15δ, 0.6δ	16.8^+	3.9^+	34^+	2048

Table 4. Characteristics of the SPIV datasets

2.2. *DNS data of turbulent channel flow*

The data of turbulent channel flow at $Re_\tau = 950$ is from DelAlamo et al [1] and was obtained by means of direct numerical simulation (DNS). The characteristics of the full DNS are summarized in table 5. All details about the simulation can be found in DelAlamo et al [1]. The Reynolds number of this DNS is comprised between that of the LTRAC dataset and that of the LML datasets. The spanwise resolution is comparable to that of the SPIV, while the streamwise resolution is coarser than in the SPIV. Of course, the SPIV data is averaged over the interrogation window size, while the DNS is free from this type of averaging.

Re_τ	S_x	S_y	S_z	Δ_x	Δ_z
950	$8\Pi h$	$2h$	$3\Pi h$	11^+	5.7^+

Table 5. Full DNS from [1]

3. Average properties

The LTRAC and LML database are validated through an analysis of some of the single point statistics such as the mean flow, the longitudinal and spanwise power spectra, and the dissipation profile. For each flow configuration, these quantities were obtained through an ensemble average over the number of records acquired, and also through an average along the homogeneous directions of the measurement planes (the streamwise direction for the XY planes, and the spanwise direction for the YZ planes). Note that the homogeneity assumption along the streamwise direction can be used because the streamwise extent of the field of view (at most $165mm$ for the LTRAC and $50mm$ for the LML) is small with respect to the total development length of the boundary layer ($3.7m$ for the LTRAC and $18m$ for the LML). The SPIV profiles are compared to theoretical laws, and to the original DNS dataset (3D and non-interpolated).

3.1. *Mean Flow*

The wall normal evolution of the mean streamwise velocity is shown for the XY and YZ planes. For the channel flow, the mean profile was computed by Hoyas and Jiménez [26] on the full DNS (see table 5).
It is plotted in external units (non dimensionalized with the free velocity U_∞ and the momentum thickness θ) in figure 4(a) and in wall units in the near-wall region in figure 4(b).
In the inner region ($y/\delta \leq 0.2$), all the data (both SPIV boundary layer and DNS channel flow) display a very good collapse in wall-units, and are in excellent

agreement with the law of the wall defined by the Van Driest law (for $0 < y^+ < 55$) and the logarithmic law (for $55 < y^+$ and $y/\delta < 0.2$). The position of the first valid mesh point in the SPIV data is at $y^+ = 15$ for $Re_\tau = \delta^+ = 820$, at $y^+ = 24$ for $Re_\tau = \delta^+ = 2590$ in the XY plane, and at $y^+ = 34$ for $Re_\tau = \delta^+ = 2590$ in the YZ plane.

In external scaling ($y/\delta \geq 0.2$), the LML boundary layer data display a good collapse in the two planes (figure 4(a)). The PIV data shows a logical Reynolds number effect, and a visible difference with the channel flow data.

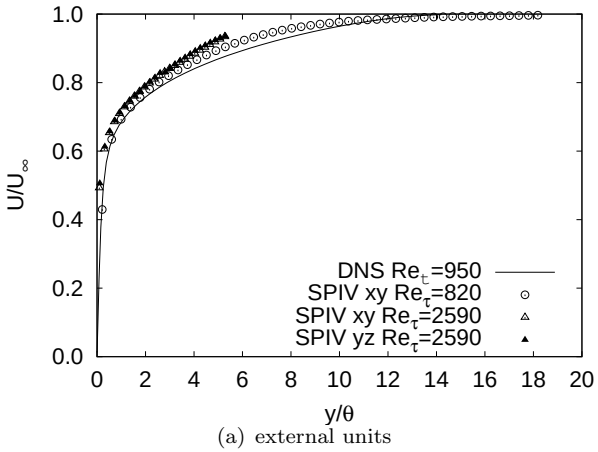

(a) external units

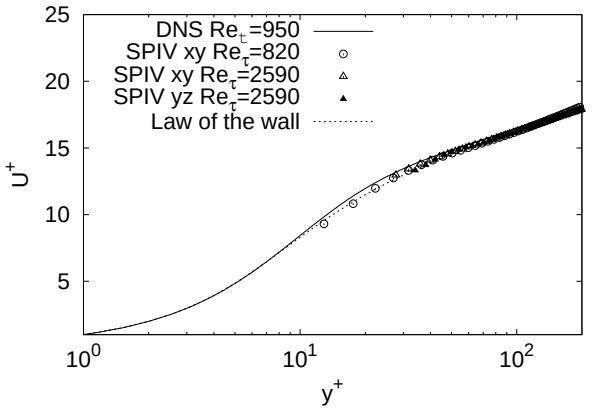

(b) wall units

Figure 4. Wall-normal evolution of mean longitudinal velocity (not every point is shown)

3.2. *Reynolds stresses*

The Reynolds stresses are the covariances of the velocity fluctuations. In Stereoscopic PIV, all the component of the Reynolds stress tensor can be retrieved, which is interesting for a comparison with the DNS data. Following the homogeneity assumption along the z direction, only the $< u'u' >$, $< v'v' >$, $< w'w' >$ and $< u'v' >$ components are non trivial, and are shown in figure 5 for the boundary layer flows (measured with SPIV) and the channel flow (obtained from DNS).

Looking first at the datasets at $Re_\tau = 2590$, it can be seen that all the Reynolds stresses obtained from the measurements in the XY and YZ planes at this Reynolds number are in excellent agreement with each other. When comparing all the

datasets, one can first notice that there is an excellent agreement on the shear component $< u'v' >$ for all Reynolds number. This component of the Reynolds stress tensor plays a key role in the production of turbulent kinetic energy. It should be noted that $< u'v' >$ is expected to remain unaffected by the PIV noise, as the noise on the u and v components is not correlated. A Reynolds number effect is clearly visible on $< v'v' >$: the datasets obtained from SPIV in the LTRAC water-tunnel and from DNS, for which the Reynolds number are close to each other ($Re_\tau = 820$ and $Re_\tau = 950$ respectively) are in quite good agreement, while those from the LML, obtained at a higher Reynolds number do not collapse so well.

As far as $< u'u' >$ is concerned, there is a clear departure between all the boundary layer flows and the channel flow in the outer region. This may be due to the difference between the nature of the two flows. Finally, the $< w'w' >$ component of the boundary layer flow at $Re_\tau = 820$ appears increasingly larger with decreasing wall-normal distance as compared to the channel flow at $Re_\tau = 950$. This is linked to the influence of the PIV noise on the out-of-plane component (see section 2.1.1). A Reynolds number effect is also visible on this component when comparing the LML and LTRAC datasets.

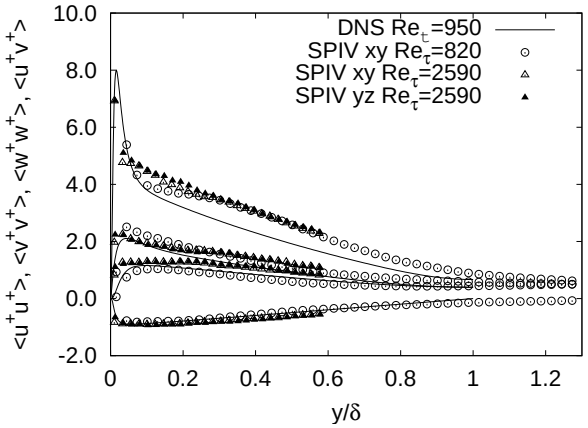

Figure 5. Wall-normal evolution of the Reynolds stresses ($< u'u' >$, $< v'v' >$, $< w'w' >$, and $< u'v' >$) (not every point is shown)

3.3. *Spectral Analysis*

Spectral analysis is of special interest to characterize turbulence which is, in essence, a multi-scale phenomenon. Here we consider only the 1D power spectra of the streamwise velocity $E_{11}(k)$ at $y^+ = 100$ along the streamwise (figure 6(a)) and spanwise (figure 6(b)) directions. The spectra have been non-dimensionalized using the inner scaling from [27] :

$$\begin{aligned} \bar{k} &= ky \\ \bar{E}(\bar{k}) &= \frac{E(ky)}{u_\tau^2} = \frac{E(k)}{u_\tau^2 y} \end{aligned} \tag{1}$$

As it can be seen, the SPIV and DNS spectra are in excellent agreement in the low ($\bar{k} < 1$) and intermediate ($1 < \bar{k} < 10$) wavenumbers range. In particular, all spectra tend to a power law of '-5/3' in the inertial subrange. In the high wavenumber domain, a spurious lift-up of the PIV spectra with respect to DNS is visible: it indicates that measurement noise becomes dominant at these scales

([5]). Taking the DNS spectrum as the reference spectrum of the flow, it is possible to compute the wavenumber $\bar{k}_{SNR=1}$ at a signal-to-noise-ratio of 1 of the SPIV (and the associated structure size, e.g. radius of a vortex that would be resolved with SNR=1) ([6]). The cut-off wavenumbers are reported on the spectra. Their values read: $\bar{k}_{SNR=1} = 12.7$ ($r^+_{SNR=1} = 25$) for the LTRAC datasets, $\bar{k}_{SNR=1} = 15.2$ ($r^+_{SNR=1} = 21$) for the LML datasets in the XY plane, and $\bar{k}_{SNR=1} = 16.6$ ($r^+_{SNR=1} = 19$) for the LML dataset in the YZ plane.
The power spectra for the v and w components are not shown, but a similar behavior to the u component was obtained, with some slight differences on the value of the cut-off wavenumber whose ordering is consistent with that of the velocity uncertainties (see section 2)

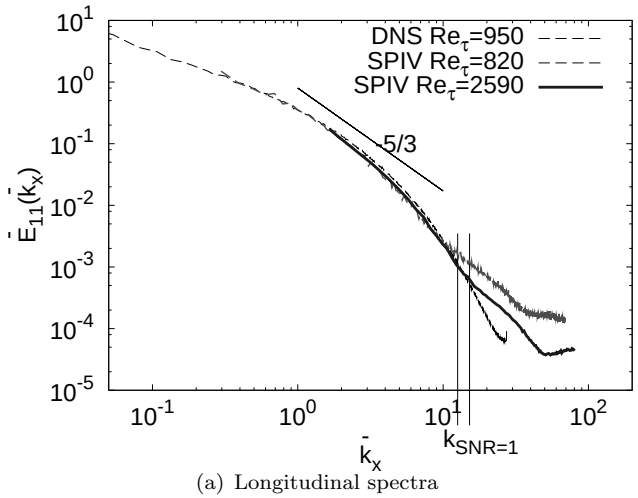

(a) Longitudinal spectra

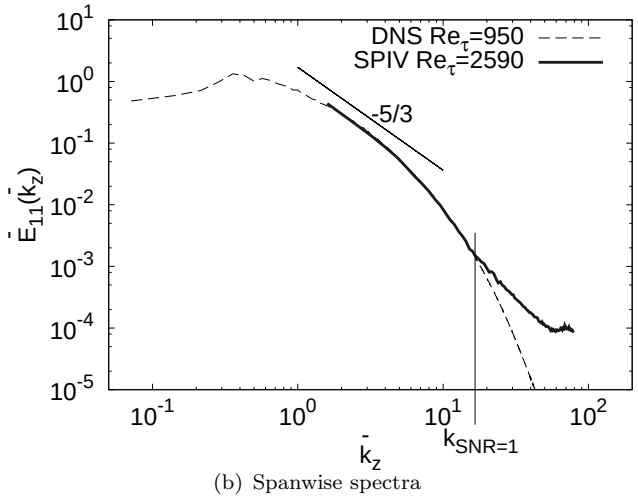

(b) Spanwise spectra

Figure 6. Power Spectra of u velocity at $y^+ = 100$

3.4. *Dissipation and Kolmogorov length scale*

In turbulence, motions exist in a wide range of sizes. However, the size of the small scale motions admits a lower bound, which is fixed by the viscosity: the Kolmogorov scales. The computation of the Kolmogorov scales requires the knowledge of the dissipation rate ϵ of the turbulent kinetic energy. The dissipation is a very hard quantity to measure, as all nine components of the fluctuating velocity gradient

tensor must be known with sufficient accuracy. When the flow is locally homogeneous and isotropic, Schlichting [28] suggested to use the following approximation:

$$\epsilon = 15\nu < \left(\frac{\partial u_1'}{\partial x_1}\right)^2 > \tag{2}$$

Shear flows can be considered as locally isotropic in most of their domain, especially for the small scales, at the exception of regions in close proximity to walls.
A convenient way to evaluate the dissipation is then to use the Taylor micro scale λ, defined as:

$$\left(\frac{\partial u_1'}{\partial x_1}\right)^2 = 2\frac{u_1'^2}{\lambda_1^2}$$

This length is representative of the *most* dissipative motions. It can be retrieved using the osculating parabola to the two-points correlation coefficient of the streamwise velocity fluctuation:

$$\lambda_1 = \sqrt{\frac{-2}{\frac{\partial R_{11}(\Delta x_1)}{\partial \Delta x_1}|_{\Delta x_1=0}}} \tag{3}$$

The dissipation and the Kolmogorov lengthscale of the LTRAC and LML boundary layer were computed at 18 wall-normal positions in the boundary layer (with a logarithmic distribution) using this methodology. They are shown in figure 7 and 8, against the dissipation in the DNS of turbulent channel flow at $Re_\tau = 950$ ([1]), computed using the 'exact' formula of the dissipation.

It is of interest to note that the dissipation and Kolmogorov scale in SPIV dataset at $Re_\tau = \delta^+ = 820$ is in excellent agreement with that of the DNS at $Re_\tau = 950$, supporting the validity of the local isotropy approximation. The peak of ϵ at the wall, visible on the DNS dataset, is quite well captured with both datasets. Some differences are visible on the dataset at $Re_\tau = \delta^+ = 2590$ (in particular on the slope of the dissipation profile) probably owing to a Reynolds number effect. This difference is confirmed by measurements at other Reynolds numbers in the LML wind-tunnel ([**?**]).

4. Vortex Detection Methodology

The different methods for identifying vortex cores in velocity vectors fields obtained from PIV have been reviewed in great details by Jeong et al [29], Adrian et al [30] and Chakraborty et al [31].
Some common intuitive criteria, such as vorticity isosurfaces and closed or spiraling streamlines and pathlines are in fact inadequate to detect vortices in turbulent boundary layers ([29]): iso-vorticity surfaces fail to identify vortex cores in shear flows, whereas closed or spiraling streamlines and pathlines, which are not Galilean invariant, are unable to detect vortices convected at different speeds. The SPIV data is planar, and the technique employed to detect vortices is based on the discriminant of the 2D velocity gradient tensor $A_{ij} = \frac{\partial u_i}{\partial x_j}$ ([32]), computed using a second order least-square derivative scheme that minimizes the propagation of measurement noise in the SPIV data ([33]). When complex eigenvalues of the tensor exist, their imaginary part, called the swirling strength ([30]), is used as a detection function of vortex cores. In wall-bounded turbulence,

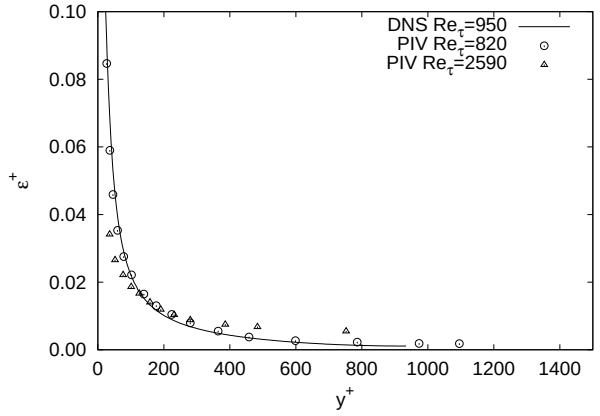

Figure 7. Wall-normal evolution of the mean dissipation, in wall units

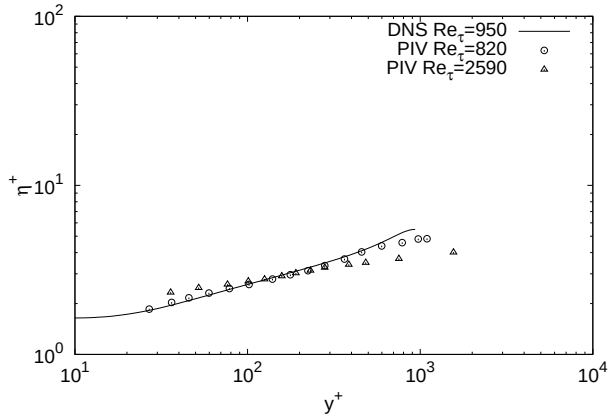

Figure 8. Wall-normal evolution of the Kolmogorov length scale, in wall units

the intensity of the detection function peaks decreases with increasing wall-normal distance ([1]). Therefore structures at the wall and away from the wall cannot be visualized using the same surface levels, as already observed by Blackburn et al [34]

In order to overcome this difficulty, a normalization is then applied to the detection function. The 2D swirling strength is divided by the wall-normal profile of its RMS value:

$$\bar{\lambda}_{ci}(x_{1/3}, x_2) = \frac{\lambda_{ci}(x_{1/3}, x_2)}{\lambda_{ci,RMS}(x_2)}$$

This type of normalization was first used by Delalamo et al [1] and Wu and Christensen [14]. The normalized function is then smoothed using a 3*3 sliding average to remove the remaining noise. Extrema exceeding a fixed threshold ($\lambda_{ci}(x_{1/3}, x_2) > 1.5\lambda_{ci,RMS}(x_2)$) are retained as center of vortex cores.

The velocity fields surrounding extrema of the detection function are then fitted to a model vortex with a non-linear least square algorithm (Levenberg-Marquardt). The model is an Oseen vortex, defined in equation 4.

$$\vec{u}(r,\theta) = \vec{u_c} + \frac{\Gamma}{2\Pi}\frac{1}{r}\left(1 - exp\left(-\left(\frac{r}{r_0}\right)^2\right)\right)\vec{e_\theta} \tag{4}$$

Plane (1-2)	h^+ Re_τ	Domain $S_{x/z}, S_y$	Mesh step Δ_i	n° records
XY	950	$8\Pi h$, h	4.5^+	342
ZY	950	$3\Pi h$, h	4.5^+	468

Table 6. Interpolated planes from the DNS dataset

This procedure has already been employed by Carlier and Stanislas [8] and Stanislas et al [16]. It validates that the structure detected is indeed a vortex, and allows the retrieval of the vortex characteristics (radius, circulation, convection velocity, sub-grid position of the center) through the fitted parameters of the model. An example of accepted vortex is shown in figure 9. It is plotted against the closest Oseen vortex obtained with the fitting procedure (the correlation coefficient between the model and the PIV field is 0.96).

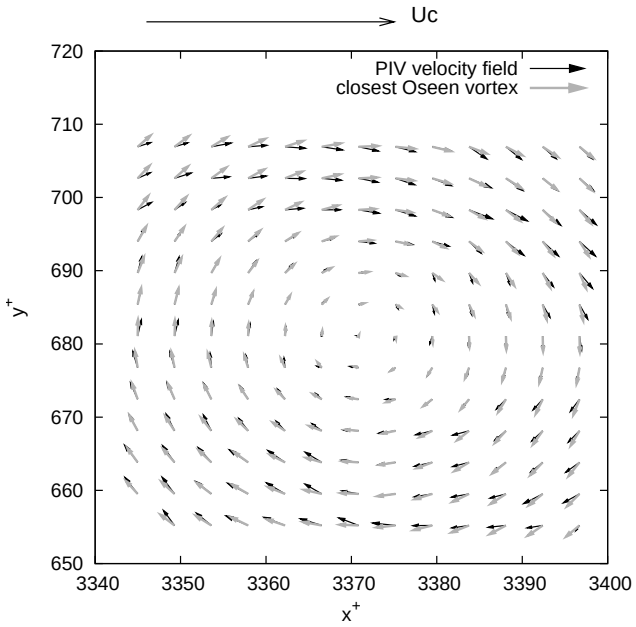

Figure 9. Comparison of a vortex and its closest Oseen model . The convection velocity (shown in black at the top of the figure) has been subtracted to the PIV velocity field.

To run this detection methodology on the DNS data from DelAlamo et al [1] as well, streamwise/wall-normal and spanwise/wall-normal planes were extracted from the 3D DNS, and interpolated on a regular mesh. The planes were extracted from nine three-dimensional velocity fields, uncorrelated in time. Successive planes are separated by a distance equal to $h^+/2$ for the XY planes and to h^+ for the YZ planes (where h is the half channel height). The interpolation was undertaken using two-dimensional bi-cubic spline interpolation. The regular mesh have a spacing of 4.5^+ in all directions. This resolution is close to the native resolution of the DNS in the spanwise direction, and is equal to the one of the LTRAC dataset. It can be seen that the native mesh spacing of the DNS in the streamwise direction is more than twice as large as the spacing used for the interpolation. In contrast, the full DNS was better resolved in the wall-normal direction. The characteristics of the interpolated XY and YZ planes of the DNS are summarized in table 6. The total number of points for the DNS planes (defined as the number of points in each plane times the records number) is roughly equal the total number of points for the SPIV dataset at $Re_\tau = \delta^+ = 2590$.

5. Results : characteristics of the vortical structures

The detection technique described above is employed to detect streamwise vortices (in the YZ planes) and spanwise vortices (in the XY planes) in the SPIV boundary layer database. It is also applied to the DNS planes at $Re_\tau = 950$ interpolated on a regular mesh (see table 6). Some statistics are computed on the characteristics of the detected vortices and analyzed.

5.1. *Density of the vortices*

The general trends for the wall-normal evolution of the vortex densities in the XY plane and in the YZ plane are first analyzed. The densities were computed for all datasets by taking into account eddies contained in layers of 25^+ in height, and normalized so that it represents the density of vortices per wall-unit square (figures 10(a), 10(b) and 10(c)). The total density of spanwise oriented vortices (detected in the XY plane), the density of prograde (spanwise vortices with rotation in the same sense as the mean shear $w_0 < 0$) and retrograde ($w_0 > 0$) vortices, and the total density of streamwise oriented vortices (detected in the YZ plane) are represented.

As can be seen, the normalized density of detected vortices is close for all three datasets, and the overall evolution with wall-normal distance is similar. The LML PIV densities are clearly less converged than the DNS ones, but the orders of magnitude are very comparable.
Looking at the global wall-normal evolution, a maximum vortex density is obtained in the near-wall-region ($y^+ \approx 60$ for the streamwise vortices, and at $y^+ \approx 150$ for the spanwise vortices), and then the density decreases with increasing wall-normal distance.
The streamwise vortices appear to be more numerous than the spanwise ones. This predominance of streamwise vortices is maximum at the wall, and then diminishes with increasing wall-normal distance. At the edge of the boundary layer (or on the channel centerline), the vortex population tends to be equally constituted of both streamwise and spanwise vortices. The fact that quasi-streamwise vortices are the major constituent of the near-wall region ($y^+ < 150$) was also observed using a λ_2 criterion by Jeong et al [35] in a DNS of channel flow at $Re_\tau = 180$ and by Sheng et al [36] in holographic 3D velocity field of a turbulent boundary layer at $Re_\tau = 1400$.
Among the spanwise vortices, the predominance of the prograde vortices is overwhelming in the inner wall region ($y^+ < 150$), and the prograde and retrograde vortex densities follow different wall-normal evolution in the outer region : the density of the prograde vortices continuously decreases with increasing wall-normal distance, while the density of the retrograde vortices stabilizes until $y/\delta = 0.5$, and then start to increase again, at a very low rate. When reaching the edge of the wall layer, the density of prograde and retrograde vortices tends to an equal level ([14]).
When comparing more closely the SPIV datasets with the DNS dataset, no significant difference appear. The agreement is especially good with the SPIV dataset at $Re_\tau = \delta^+ = 2590$, whereas the dataset at $Re_\tau = \delta^+ = 820$ seem to contain a lower number of vortices. This may be linked to a low Reynolds number effect.

5.2. *Radius of the vortices*

The wall-normal evolution of the mean radius is plotted in figure 11(a) for the spanwise vortices (XY plane), and in figure 11(b) for the streamwise vortices (YZ

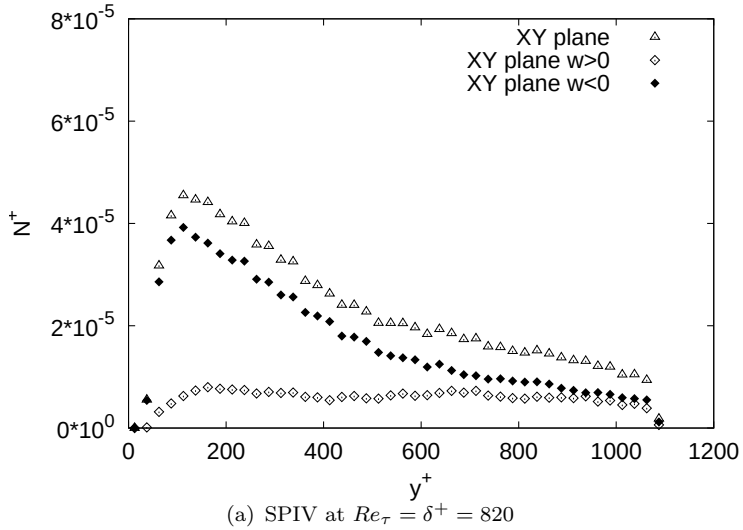

(a) SPIV at $Re_\tau = \delta^+ = 820$

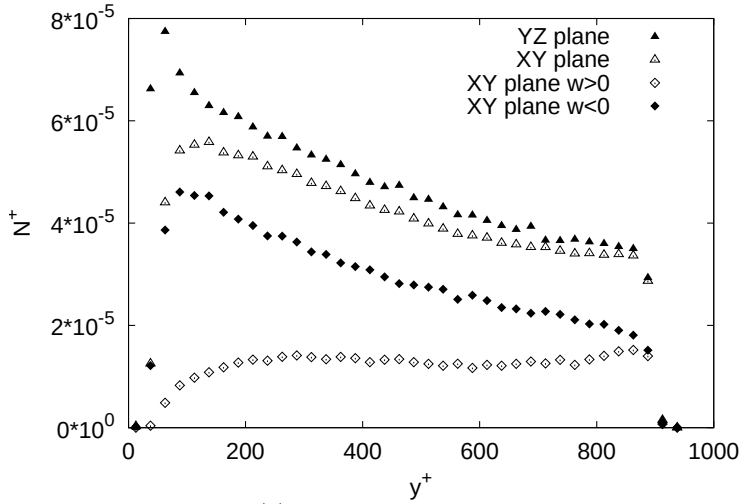

(b) DNS at $Re_\tau = 950$

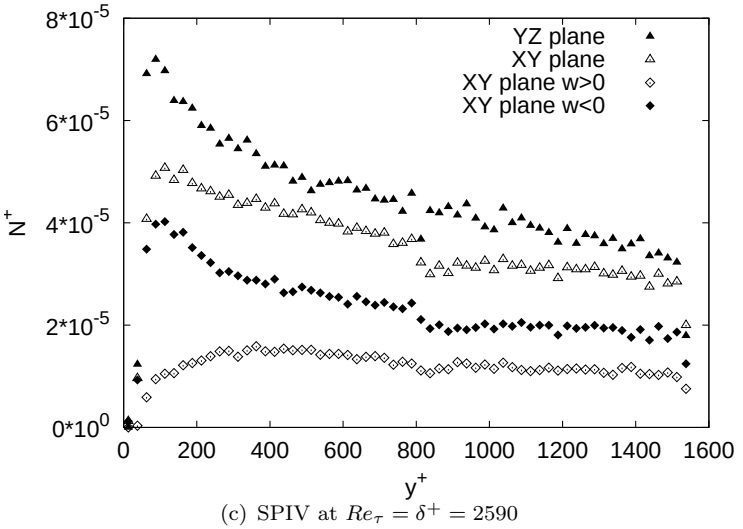

(c) SPIV at $Re_\tau = \delta^+ = 2590$

Figure 10. Wall-normal evolution of mean vortex density

plane), in wall units. It was computed for all datasets by taking into account eddies contained in layers of 25^+ in height. For both types of vortices, a good universality

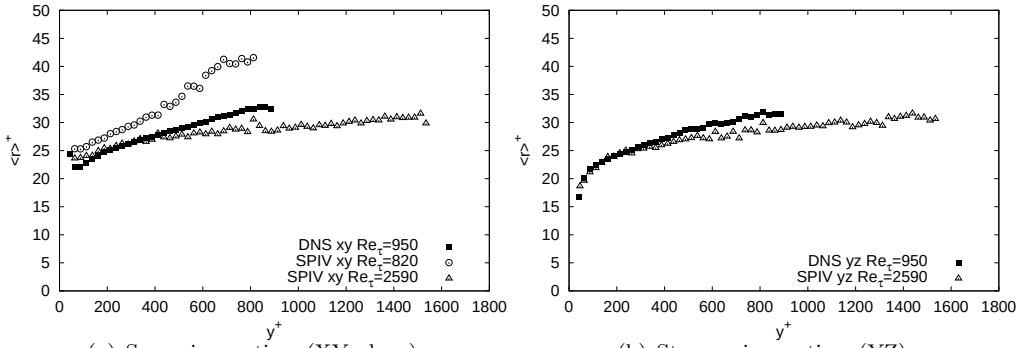

(a) Spanwise vortices (XY plane) (b) Streamwise vortices (YZ)

Figure 11. Wall-normal evolution of the mean radius, in wall units

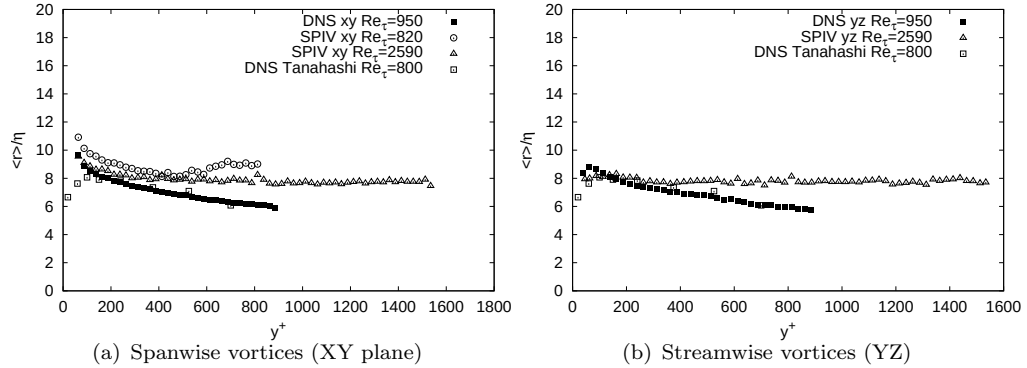

(a) Spanwise vortices (XY plane) (b) Streamwise vortices (YZ)

Figure 12. Wall-normal evolution of the mean radius, in Kolmogorov units

is obtained in the inner region, but a Reynolds number effect is clearly visible in the outer region. In the XY plane, the radius appears to be slowly increasing with wall normal distance over the whole field, except for the dataset at $Re_\tau = \delta^+ = 820$ where a steep increase of mean radius is observed for $y^+ > 400 \Leftrightarrow y/\delta > 0.5$. This may be due to intermittency with the free stream; as can be seen in the previous section 5.1, the density of vortices for that dataset in the region $y/\delta > 0.5$ is quite low, and therefore this part of the profile may not be really meaningful. In the YZ plane, the behavior of the mean radius is quite different. Two regions must be distinguished: the region $y^+ < 100$, where the radius increases strongly with wall-normal distance, and the region $y^+ > 100$, where the radius increases slowly with wall-normal distance toward a value of 30^+. Therefore the streamwise vortices (detected in the YZ plane) are found to be smaller than the spanwise vortices (detected in the XY plane) in the near wall region. This may indicate that, being inclined to the wall, the streamwise vortices are stretched by the mean velocity gradient. All vortices (except those of the dataset at $Re_\tau = \delta^+ = 820$) tend to mean radius of 30^+ toward the edge of the boundary layer or the channel centerline.

The wall-normal evolution of the mean radius scaled with the Kolmogorov length scale is plotted in figure 12(a) for the spanwise vortices (XY plane) and in figure 12(b) for the streamwise vortices (YZ plane). The Kolmogorov length scale used for the normalization of each dataset is the one shown and analyzed in section 3.4. For the SPIV data of BL flow, the radius in Kolmogorov scaling is roughly independent of wall-normal distance in the region $y^+ > 150$ and equal to

8η for the spanwise vortices and all across the layer for the streamwise vortices. A different trend is noticeable for the DNS data of channel flow of DelAlamo et al [1]. In both planes, the mean radius is found to decrease slowly with increasing wall-normal distance, and no constant value of r/η is reached. However, the mean radius of the SPIV and of the DNS are still on the same order. The SPIV and DNS data post-processed with our detection algorithm is also compared here with the DNS data from Tanahashi et al [17] at $Re_\tau = 800$, post-processed with their own 3D detection algorithm. The mean radius is obtained by integration of the PDF of the radius shown in [17]. As can be seen, the mean radius obtained by Tanahashi et al [17] is in good agreement with the one computed on the data of DelAlamo et al [1] with our vortex detection algorithm, especially for the streamwise vortices.

It is of interest to examine not only the mean values but also the distributions of the vortex radius. The PDF of the vortex radius are computed in the logarithmic region at different wall-normal positions (computed over adjacent layers of 50^+ in height), and then superimposed for the different wall-normal positions and Reynolds number of the flow.

The PDF in the logarithmic region are studied in two different scalings :

- the wall-units scaling (figures 13 and 14)
- the Kolmogorov scaling (figures 15 and 16)

For each scaling the PDF of the radius is normalized such that equation 5 is verified for each layer of 50^+ in height centered at y (variable $\bar{r}$ stands for the non-dimensional radius, and variable P_y stands for the probability density function of $\bar{r}$ in the layer centered at y).

$$\int_{\bar{r}} P_y\left(\bar{r}\right) d\left(\bar{r}\right) = 1 \tag{5}$$

The PDF of the vortex radius in wall-units (figures 13 and 14) show that vortices with radius in the range $[10^+; 80^+]$ are found. The collapse of the PDF is not so bad, however a shift between the datasets at different wall-normal position is clearly visible, The most probable radius is comprised between 16^+ and 24^+.

In Kolmogorov scaling, the overall agreement of the PDFs throughout the logarithmic region appear better for both the XY planes and the YZ planes (see figures 15 and 16). Vortices with radius in the range $[2\eta; 30\eta]$ are found.
A very good collapse of the PDF for the spanwise (detected in the XY plane) and streamwise (detected in the YZ plane) vortices is observed in the lowest range of radius, and in both PIV and DNS data. In particular, the most probable radius is found to be universal for all Reynolds numbers and for both type of vortices, at a value of 7η. A good collapse of the radius PDF was also observed by Stanislas et al [16] in YZ planes of turbulent boundary layers at $Re_\theta = 7800$ and $Re_\theta = 15000$ in Kolmogorov scaling (in the logarithmic region). However, some scatter of the PDF is visible for large radius ($r/\eta > 13$), indicating a lack of universality for the largest vortices detected and also probably a lack of convergence due to the limited sample size. It was checked that the use of external units (e.g. momentum thickness) do not provide a better collapse of the PDF for the large vortices (the collapse is actually worse over the whole range of radius investigated).
The PDF in the outer region are not shown here. The shape still look similar but the collapse in the Kolmogorov scaling deteriorates as the distance from the wall increases.
Another possible internal scale for the PDF is the Taylor micro-scale. This scaling

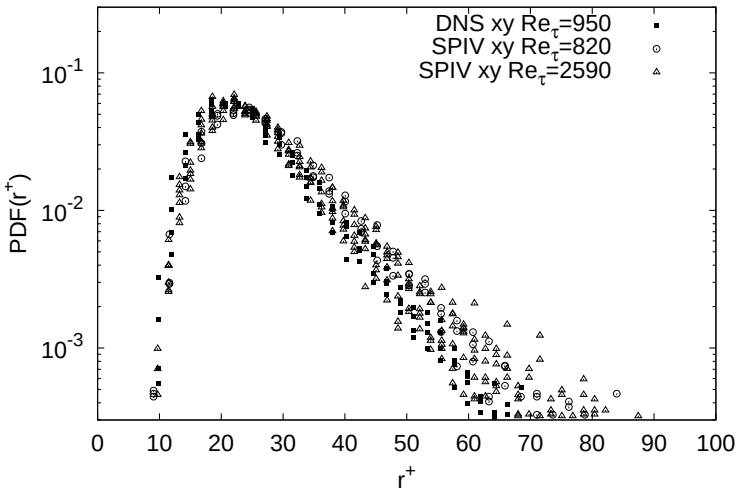

Figure 13. PDF of radius of the spanwise vortices (detected in the XY plane) in the logarithmic layer ($100 < y^+$ and $y/\delta < 0.25$) in wall-units scaling

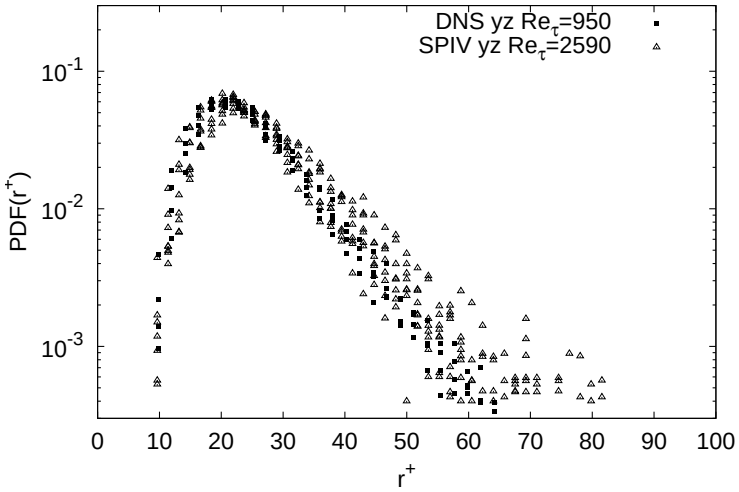

Figure 14. PDF of radius of the streamwise vortices (detected in the YZ plane) in the logarithmic layer ($100 < y^+$ and $y/\delta < 0.25$) in wall-units scaling

was tested, but the collapse of the PDF is not as good as for the Kolmogorov scaling.

5.3. *Vorticity of the vortices*

The wall normal evolution of the absolute mean value of vorticity at the center of the vortices is represented in figure 17(a) for the spanwise vortices (XY plane) and in figure 17(b) for the streamwise vortices (YZ plane), in wall units. It was computed for all datasets by taking into account eddies contained in layers of 25^+ in height. As can be seen, in both planes, the vorticity decreases with increasing wall normal distance. The rate of decay is very strong close to the wall, and then diminishes with increasing wall-normal distance. In the near wall region ($y^+ < 250$) a good collapse of the vorticity in all datasets and in both planes is observed. At the wall, the profile of vorticity of the streamwise vortices is tangent to the velocity gradient dU^+/dy^+ given by the Van Driest law. The peak of vorticity at the wall is slightly higher in the YZ plane than in the XY plane. This may indicate that the streamwise vortices (detected in the YZ plane) are more intensified by the mean velocity gradient than the spanwise vortices (detected in the XY plane). A

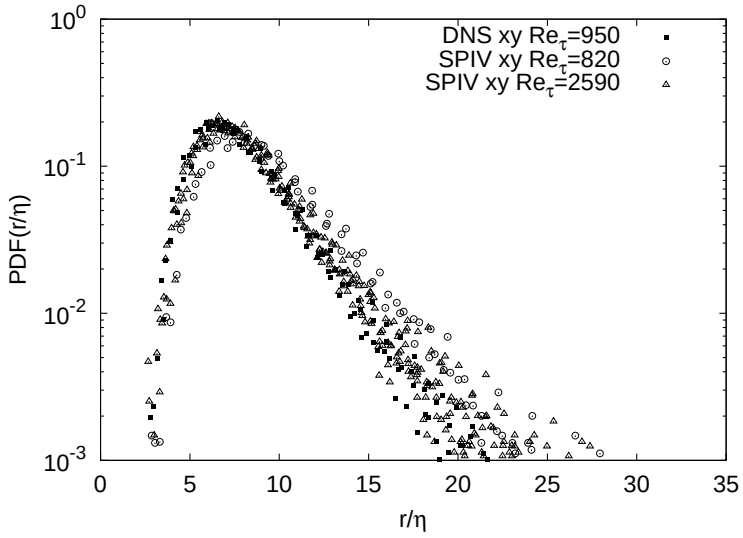

Figure 15. PDF of radius of the spanwise vortices (detected in the XY plane) in the logarithmic layer ($100 < y^+$ and $y/\delta < 0.25$) in Kolmogorov scaling

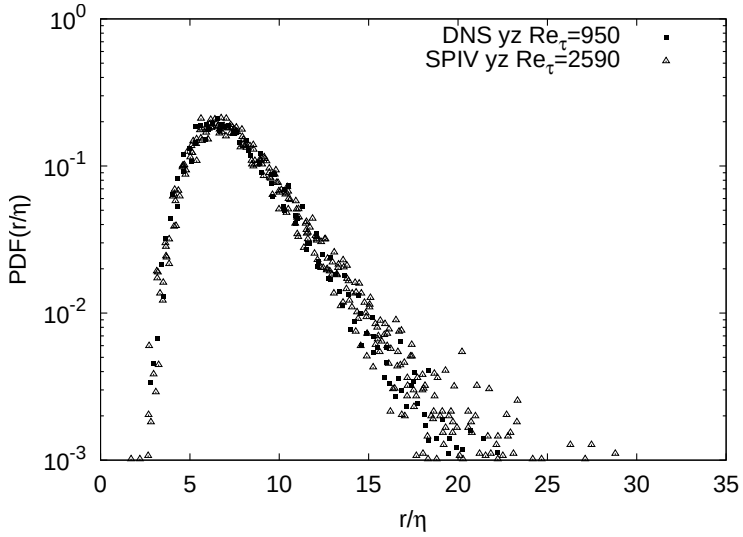

Figure 16. PDF of radius of the streamwise vortices (detected in the YZ plane) in the logarithmic layer ($100 < y^+$ and $y/\delta < 0.25$) in Kolmogorov scaling

Reynolds number effect is visible in the outer region. No specific behavior of the DNS data of channel flow is noted.

The wall-normal evolution of the mean vorticity scaled with the inverse of the Kolmogorov time scale is plotted in figure 18(a) for the spanwise vortices (XY plane) and in figure 18(b) for the streamwise vortices (YZ plane). The behavior is similar in the two planes. The quantity $< w_0 > \tau$ appears to be quite constant in the upper buffer layer and in the logarithmic region of the SPIV datasets, and across the whole wall layer of the DNS dataset. The vorticity appears about 20% stronger in the DNS of channel flow than in the SPIV of BL flow.

The vorticity distribution of the vortices in the flow is also analyzed. In the logarithmic region, the rate of decay of the mean vorticity with wall-normal distance in wall-units scaling (figures 17(a) and 17(b)) is so strong that the PDF cannot be universal in wall-units. Accordingly, the PDF are shown in Kolmogorov scaling only.

In the same fashion as for the radius, the probability density functions $P_y(\omega_0\tau)$ are computed over each layer of 50^+ in height in the logarithmic region following

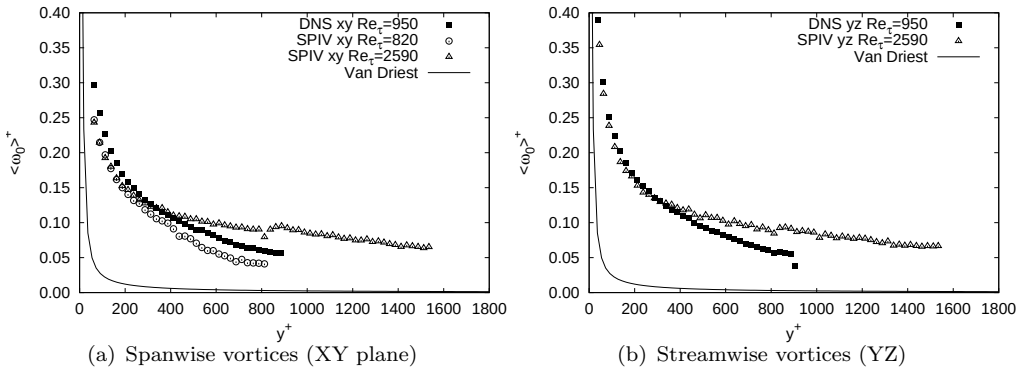

(a) Spanwise vortices (XY plane) (b) Streamwise vortices (YZ)

Figure 17. Wall normal evolution of mean vorticity, in wall-units

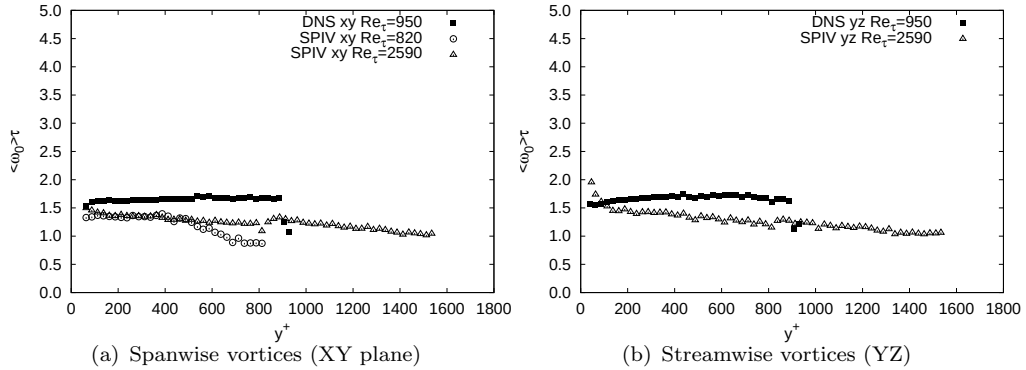

(a) Spanwise vortices (XY plane) (b) Streamwise vortices (YZ)

Figure 18. Wall-normal evolution of the mean vorticity, in Kolmogorov units

equation 6, and then superimposed.

$$\int_{\omega_0\tau} P_y\left(\omega_0\tau\right) d\left(\omega_0\tau\right) = 1 \tag{6}$$

The overall agreement of the PDF between the PIV and the DNS data throughout the logarithmic region is good for both the XY planes and the YZ planes (see figures 19 and 20). The vorticity at the center of the vortices is found to be in the range $[0.25\tau^{-1}; 8\tau^{-1}]$. In both planes, excellent agreement between the various datasets is found in the small and intermediate vorticity range ($w_0\tau \in [0.25; 3]$). In particular, the most probable value of the vorticity at the center of the vortices is $w_0\tau = 0.9$. In the large vorticity range, some differences are noted; more vortices with large vorticity are detected in the DNS dataset, which is consistent with the higher value of mean vorticity that was found (see figures 18(a) and 18(b)).
The PDF in the outer region are not shown here. The shape still look similar but the collapse in the Kolmogorov scaling deteriorates as the distance from the wall increases.

6. Discussion and Conclusions

As stated by Robinson [4], the study of streamwise and spanwise vortices *'lies at the heart of turbulent boundary layer research [...] because [these vortices] have the potential to function as a pump that transports mass and momentum across the mean velocity gradient'*.
In this contribution, the streamwise and spanwise vortices in boundary layer

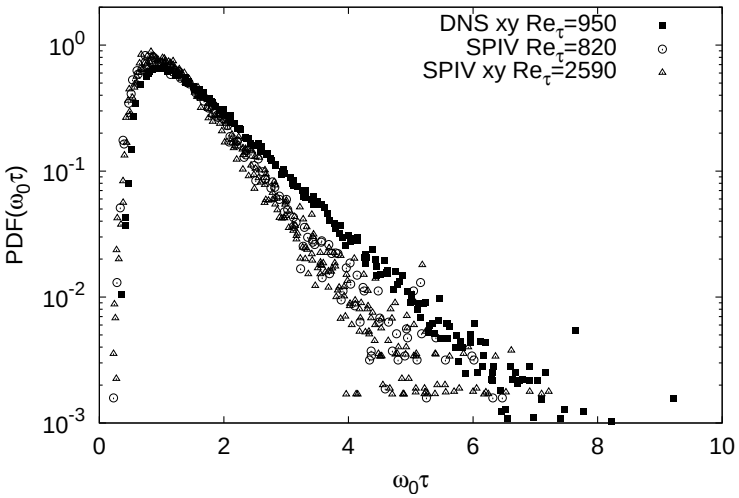

Figure 19. PDF of vorticity of the spanwise vortices (XY plane) in the logarithmic layer ($100 \leq y^+$ and $y/\delta < 0.25$)

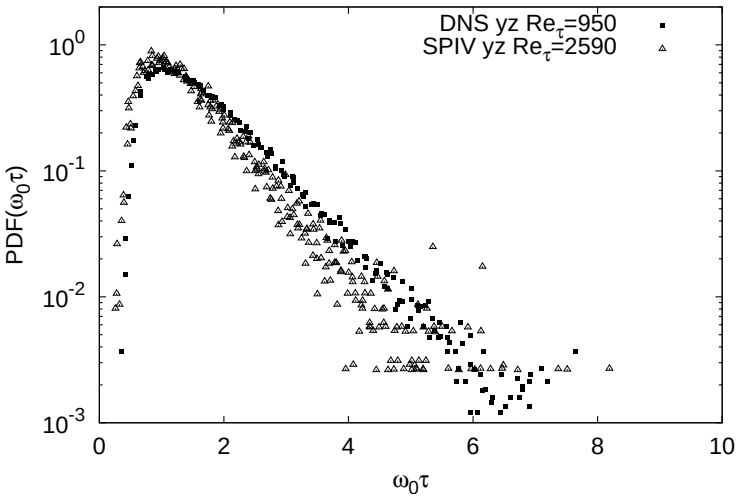

Figure 20. PDF of vorticity of the streamwise vortices (YZ plane) in the logarithmic layer ($100 \leq y^+$ and $y/\delta < 0.25$)

and channel flow at moderate Reynolds number obtained from SPIV in the LTRAC water-tunnel ($Re_\tau = \delta^+ = 820$, XY plane) and in the LML wind-tunnel ($Re_\tau = \delta^+ = 2590$, XY and YZ plane) as well as in DNS data from DelAlamo et al [1] at $Re_\tau = 950$ were analyzed and compared. The measurement uncertainty of the SPIV data was assessed and is quite low (1.5% of U_∞ at most), as required for the study of the fine-scale eddies.

The SPIV datasets were validated through the analysis of the mean velocity profile and the power spectra, that were compared with reference profiles derived from theory and DNS data. The SPIV mean velocity profile show excellent agreement with the law of the wall in the inner region, down to the first measured points which are obtained between $y^+ = 13$ and $y^+ = 34$ depending on the dataset. The SPIV and DNS spectra are in good agreement, except in the high wavenumber region, where the influence of measurement noise is visible in PIV. In order to detect vortices in the DNS data with the same detection algorithm as in the SPIV data, XY and YZ plane were extracted from the 3D domain of the DNS, and interpolated on a regular mesh. The resolution of the interpolated DNS planes is 4.5^+, which is close to the resolution of the SPIV data.

The vortex detection algorithm employed is based on the 2D swirling strength and

on a fit of an Oseen vortex model, which allows to retrieve the vortex characteristics, including its radius, vorticity, and position of the center.

The density of the streamwise and spanwise vortices as a function of wall-normal distance was first analyzed. The near-wall region ($y^+ \leq 150$), comprised of the upper buffer-layer and innermost part of the logarithmic layer, was found to be predominantly populated with quasi streamwise vortices, in agreement with previous findings of Robinson [4], Jeong et al [35], Carlier and Stanislas [8] and Sheng et al [36]. A maximum vortex density is obtained around $y^+ = 60$ for the streamwise vortices, and at $y^+ = 150$ for the spanwise vortices. The outer region is equally populated with of both types of vortices, which densities are found to decrease slowly with increasing wall-normal distance. No significant difference was found between the SPIV and the DNS data.

The vortex radii were then investigated. In wall units, a good collapse is obtained in the inner region, but some differences are clearly visible in the outer region, consistent with a Reynolds number effect for the experimental data. The streamwise vortices appear thinner than the spanwise ones in the region $y^+ < 100$, which may indicate a stretching by the mean velocity gradient. The Kolmogorov scaling was then tested. It was first checked that the dissipation and Kolmogorov lengthscale of the SPIV is in good agreement with that of the DNS. It is especially true for the DNS and LTRAC data which have nearly the same Reynolds number and external turbulence. A slope difference appears in the LML data where the Reynolds number is higher and the external turbulence lower. For the SPIV data of BL flow, the radius in Kolmogorov scaling is roughly independent of wall-normal distance in the region $y^+ > 150$ for the spanwise vortices and all across the layer for the streamwise vortices. It is equal to 8η in both cases. A clear difference of the DNS dataset is visible: the radius do not seem constant with wall-normal distance, and slowly decreases with wall-normal distance between $y^+ = 50$ (where a value of 9η is obtained) and the channel centerline (where a value of 6η is obtained). It is of interest to note that these results obtained on the DNS of DelAlamo et al [1] are in very good agreement with those obtained by Tanahashi et al [17] on DNS data of a channel flow at $Re_\tau = 800$. This difference between the SPIV and the DNS may be linked to a difference between the boundary layer flow and the channel flow, rather than to the techniques themselves. Finally the PDF were investigated in the logarithmic region in Kolmogorov scaling. An excellent collapse of the SPIV and DNS datasets was obtained, with a most probable radius of 7η. Some differences were observed in the PDF in the range of large radii.

The same analysis was undertaken on the vorticity at the center of the vortices. In wall-units scaling, the vorticity decreases exponentially with the wall normal distance, and is tangent at the wall to the velocity gradient dU^+/dy^+ given by the Van Driest law. In the near wall region ($y^+ < 250$) a good collapse of the vorticity in all datasets and in both planes is observed, while some clear Reynolds number effect are visible in the outer region. No specific behavior of the DNS with respect to the SPIV is observed. In Kolmogorov scaling, the vorticity is quite constant in the upper buffer layer and in the logarithmic region of the SPIV datasets, and across the whole wall layer of the DNS dataset. The vorticity appears about 20% stronger in the DNS of channel flow than in the SPIV of BL flow. The PDF in Kolmogorov scaling in the logarithmic region show excellent agreement for all datasets, with a most probable value of $0.9\tau^{-1}$.

As was observed in the presentation of the results, the pdf of the radius and vorticity of the vortices, scaled by the Kolmogorov length scale, shows a significant asymmetry. Different statistical laws can be tried to represent this distribution. Among them, one of choice is the log-normal law given by the following equation:

	r/η	$\omega.\tau$
μ	2.025	0.17
σ	0.315	0.5
median	7.58	1.18
variance	6,61	0,51
asymmetry	1,00	1,75

Table 7. main parameters log-normal law fitted to PDFs of the vortices

$$pdf(x,\mu,\sigma) = \frac{1}{x\sigma\sqrt{2\pi}} exp\left(-\frac{[ln(x)-\mu]^2}{2\sigma^2}\right) \tag{7}$$

where μ and σ are two parameters characterizing the median and the variance respectively.

This law was first suggested by [2] to represent the fluctuations of the turbulent kinetic energy dissipation :

$$\epsilon = \frac{\nu}{2}\sum_{\alpha}\sum_{\beta}\left(\frac{\partial u_\alpha}{\partial x_\beta} + \frac{\partial u_\alpha}{\partial x_\beta}\right)^2 \tag{8}$$

as an improvement of his original 1941 theory ([37]).

Different other laws were tried without success. The log normal law appears the one representing at best the vortices characteristics distributions. The present fit was performed on the results at $Re_\theta = 7630$ for which the vortices are resolved at best. Figure 21 gives the pdf and the cumulative distribution compared to the log-normal law for the vortex radius. The pdf is plotted logarithmically to better see the details. The best parameters are: $\mu = 2.025$ and $\sigma = 0.315$. As can be observed, apart for a slight underestimation around the peak, the agreement is quite good on the cumulative point of view but the pdf is not so well represented by the model for the large values of r/η.

The result for the vorticity is shown in figure 22, again in both pdf (in log) and cumulative representation. Here the best parameters are : $\mu = 0.17$ and $\sigma = 0.5$. The results much better than for the radius. The fit is quite good all over the range in both pdf and cumulative representations.

It should be recalled here that the dissipation in Kolmogorov's theory is tightly linked to the vortices embedded in turbulence, and the vorticity of the vortices measured here is in direct link to the fluctuation of vorticity defined by Kolmogorov in equation 8 above. it is thus of interest to note that this "fluctuating vorticity" follows relatively faithfully the log-normal law. Nothing in the theory indicates that the size of the vortices embedded in turbulence should follow the same law. It is not so far but does not follows so faithfully. This result on the vorticity calls for further analysis as a function of the Reynolds number, as the Kolmogorov theory supposes that at high enough Reynolds number, the dispersion σ^2 of the logarithm of ϵ should become independent of the Reynolds number. The same should be true for the vortices characteristics, in particular for their vorticity.

Looking globally at the results, in wall units scaling, a good coherence in vortex densities between the different datasets is observed, as far as the wall normal distribution is concerned. These distributions support the hypothesis that the streamwise and the prograde spanwise vortices are generated near the wall, at a wall-distance

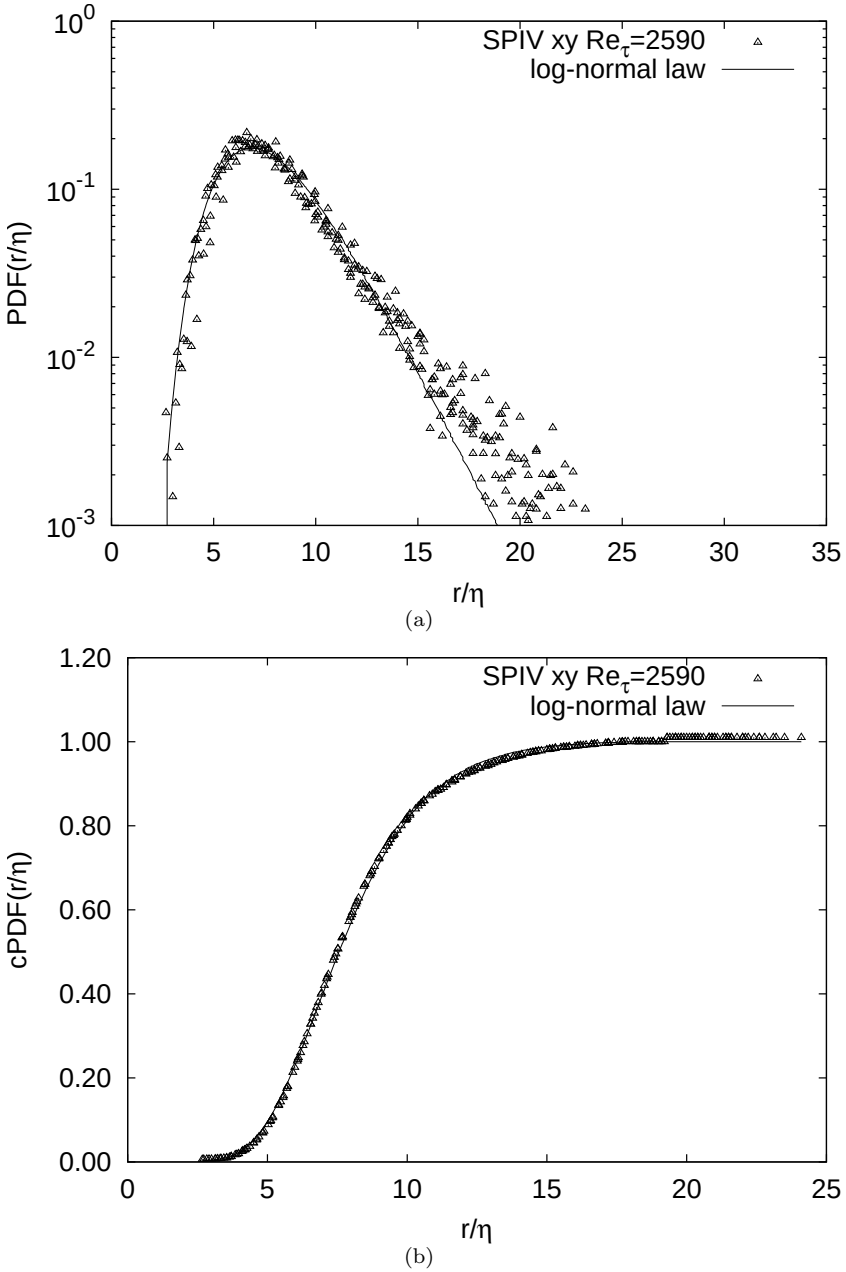

Figure 21. Probability density function of the vortices radius at $Re_\theta = 7\ 630$ compared to the log normal distribution in pdf and cumulative representation

estimated to 30^+ by Lin [38] This is strongly supported by the vorticity of these vortices, which tends to the mean velocity gradient as the wall is approached (figures 17(a) and 17(b)). Away from the wall, the behavior is coherent with the idea of vortices moving away from the wall, and diminishing in number and intensity while growing in size (in the wall-units representation). In both the wall-unit and the Kolmogorov representation, the radius of the vortices in the LTRAC data appears slightly larger than in the other datasets. This could be attributed most probably to a low Reynolds number effect, where the vortices would keep their intensity but would be less stretched and more subject to viscous diffusion leading to larger radius. This should be linked also to the fact that the population being a bit lower (10(a)), the vortices have more room to spread. Another possibility is that the higher external turbulence level influences the size of the vortices in the

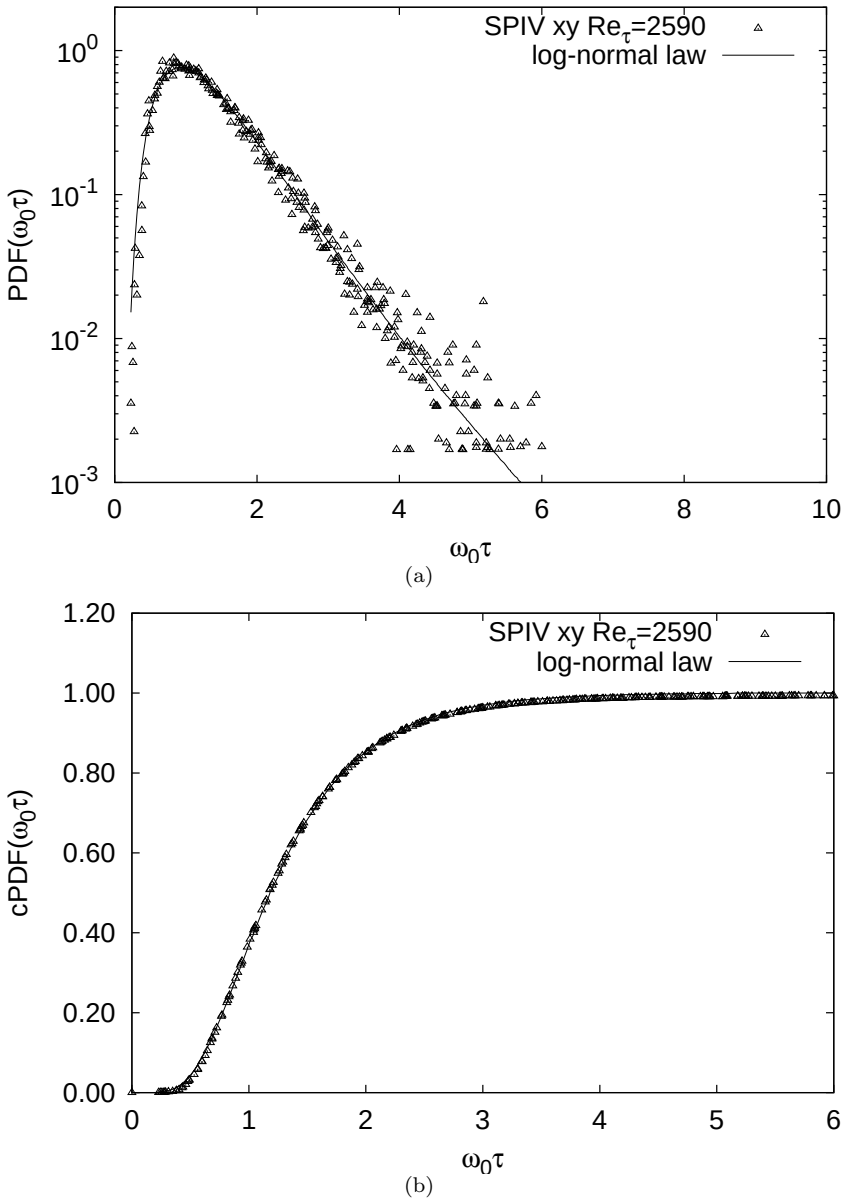

Figure 22. Probability density function of the vortices vorticity at $Re_\theta = 7\ 630$ compared to the log normal distribution in pdf and cumulative representation

outer part ($y^+ \geq 500$).

In Kolmogorov scaling, a clear difference appears between the boundary layer and the channel flow data. A first idea is to attribute it to the difference in Kolmogorov length scale observed in figure 8. But in fact, the LTRAC data is in very good agreement with the DNS data for η and coherent with the LML data for the proposed scaling - what appears is the the channel flow shows more vortices with large $\omega_0\tau$ and small r/η than the boundary layer. On average, in the DNS, the vortices decrease in r/η with increasing wall-normal distance while keeping $\omega_0\tau$ constant. In the PIV, r/η is kept nearly constant, while $\omega_0\tau$ shows a slight tendency to decrease. This difference can only be attributed to the difference in type of flow. In one case (channel flow), two wall layers interact, while in the other (boundary layer) the wall layer develops in the free-stream. This does not seem to influence the near-wall region, but may explain the difference in mean velocity observed in figure 4(a). It may also support the idea that the theoretical results should be

different for these two types of flow, at least in the upper part of the log layer and in the outer region.
Having all the vortices detected individually, the next interesting step is to post process the data in order to look at the spatial relation between these vortices. This would allow to bring a more quantitative support to the vortex packet theory mentioned in the introduction. This is planned as a next step of the present research.

Acknowledgments

Financial support from CNRS, 'Region Nord pas de Calais', the Australian Research Council, as well as 'Ecole Centrale de Lille', and the french embassy in Australia is gratefully acknowledged.

References

[1] J.C. DelAlamo, J. Jiménez, P. Zandonade, and R.D. Moser, *Self-similar vortex clusters in the turbulent logarithmic region*, J. Fluid Mech. 561 (2006), pp. 329–358.
[2] A.N. Kolmogorov, *A refinement of previous hypothesis concerning the local structure of turbulence in a viscous incompressible fluid at high Reynolds number*, J. Fluid Mech. 13 (1962), pp. 82–85.
[3] B. Cantwell, *Organized motion in turbulent flow*, Annu. Rev. Fluid Mech. 13 (1981), pp. 437–515.
[4] S.K. Robinson, *Coherent motions in the turbulent boundary layer*, Annu. Rev. Fluid Mech. 23 (1991), pp. 601–639.
[5] J.M. Foucaut, J. Carlier, and M. Stanislas, *PIV optimization for the study of turbulent flow using spectral analysis*, Meas. Sci. Technol. 15 (2004), pp. 1046–1058.
[6] S. Herpin, C.Y. Wong, M. Stanislas, and J. Soria, *Stereoscopic PIV measurements of a turbulent boundary layer with a large spatial dynamic range*, Exp Fluids 45 (2008), pp. 745–763.
[7] R.J. Adrian, C. Meinhart, and C. Tomkins, *Vortex organization in the outer region of the turbulent boundary layer*, J. Fluid Mech. 422 (2000), pp. 1–54.
[8] J. Carlier, and M. Stanislas, *Experimental study of eddy structures in a turbulent boundary layer using particle image velocimetry*, J. Fluid Mech. 535 (2005), pp. 143–188.
[9] B. Ganapathisubramani, E. Longmire, and I. Marusic, *Experimental investigation of vortex properties in a turbulent boundary layer*, Physics of Fluids 18 (2006), pp. 05510501–05510514.
[10] J. Zhou, R.J. Adrian, S. Balachander, and T.M. Kendall, *Mechanisms for generating coherent packets of hairpin vortices in channel flow*, J. Fluid Mech. 387 (1999), pp. 353–396.
[11] C.D. Tomkins, and R.J. Adrian, *Spanwise structure and scale growth in turbulent boundary layers*, J. Fluid Mech. 490 (2003), pp. 37–74.
[12] B. Ganapathisubramani, E. Longmire, and I. Marusic, *Characteristics of vortex packets in turbulent boundary layers*, J. Fluid Mech. 478 (2003), pp. 35–46.
[13] J. Lin, J.P. Laval, J.M. Foucaut, and M. Stanislas, *Quantitative characterization of coherent structures in the buffer layer of near-wall turbulence. Part 1: streaks*, Exp Fluids 45 (2008), pp. 999–1013.
[14] Y. Wu, and K.T. Christensen, *Population trends of spanwise vortices in wall turbulence*, J. Fluid Mech. 568 (2006), pp. 55–76.
[15] N. Saikrishnan, I. Marusic, and E. Longmire, *Assessment of dual plane PIV measurements in wall turbulence using DNS data*, Exp Fluids 41 (2006), pp. 265–278.
[16] M. Stanislas, L. Perret, and J.M. Foucaut, *Vortical structures in the turbulent boundary layer: a possible route to a universal representation*, J. Fluid Mech. 602 (2008), pp. 327–342.
[17] M. Tanahashi, S.J. Kang, T. Miyamoto, S. Shiokawa, and T. Miyauchi, *Scaling Law of fine scale eddies in turbulent channel flow up to* $Re_\tau = 800$, Int. J. Heat and Fluid Flow 25 (2004), pp. 331–340.
[18] S.K. Das, M. Tanahashi, K. Shoji, and T. Miyauchi, *Statistical properties of coherent fine eddies in wall-bounded turbulent flows by direct numerical simulation*, Theor. Comput. Fluid Dyn. 20 (2006), pp. 55–71.
[19] S.J. Kang, M. Tanahashi, and T. Miyauchi, *Dynamics of fine scale eddy clusters in turbulent channel flows*, J. of Turbulence 8 (2007).
[20] J. Kostas, *An experimental investigation of the structure of a turbulent backward facing step flow*, Monash Uni., 2002.
[21] S. Herpin, *Study of the influence of the Reynolds number on the organization of wall-bounded turbulence*, Ecole Centrale de Lille and Monash University, 2009.
[22] K. Parker, K. Ellenriedervon , and J. Soria, *Using stereo multigrid (SMDPIV) measurements to investigate the vortical skeleton behind a finite-span flapping wing*, Exp Fluids 39 (2005), pp. 281–298.
[23] M. Raffel, C. Willert, S.T. Wereley, and J. Kompenhans *Particle image velocimetry – a practical guide, 1st edition*, Springer, Germany, 1998.
[24] J. Carlier, *Etude des structures coherentes de la turbulence de paroi a grand nombre de Reynolds par velocimetrie par images de particules*, Universite des Sciences et des Technologies de Lille, 2001.

[25] A.K. Prasad, *Stereoscopic particle image velocimetry*, Exp Fluids 29 (2000), pp. 103–116.
[26] S. Hoyas, and J. Jiménez, *Reynolds number effects on the Reynolds stress budgets in turbulent channels*, Physics of fluid 20 (2008).
[27] A.E. Perry, S. Henbest, and M.S. Chong, *A Theoretical and experimental study of wall turbulence*, J. Fluid Mech. 165 (1986), pp. 163–199.
[28] H. Schlichting, and K. Gersten *Boundary layer theory, 8th revised and enlarged edition*, , 2001.
[29] J. Jeong, and F. Hussain, *On the identification of a vortex*, J. Fluid Mech. 285 (1995), pp. 69–94.
[30] R.J. Adrian, K.T. Christensen, and Z.C. Liu, *Analysis and interpretation of instantaneous turbulent velocity fields*, Exp Fluids 29 (2000), pp. 275–290.
[31] P. Chakraborty, S. Balachandar, and R. Adrian, *On the relationships between local vortex identification schemes*, J. Fluid Mech. 535 (2005), pp. 189–224.
[32] M.S. Chong, and A.E. Perry, *A general classification of three-dimensional flow fields*, Phys. Fluids 5 (1990), pp. 765–777.
[33] J.M. Foucaut, and M. Stanislas, *Some considerations on the accuracy and frequency response of some derivative filters applied to particle image velocimetry vector fields*, Meas. Sci. Technol. 13 (2002), pp. 1058–1071.
[34] H.M. Blackburn, N.N. Mansour, and B.J. Cantwell, *Topology of fine-scale motions in turbulent channel flow*, J. Fluid Mech. 310 (1996), pp. 269–292.
[35] J. Jeong, F. Hussain, W. Schoppa, and J. Kim, *Coherent structures near the wall in a turbulent channel flow*, J. Fluid Mech. 332 (1997), pp. 185–214.
[36] J. Sheng, E. Malkiel, and J. Katz, *Using digital holographic microscopy for simultaneous measurements of 3D near wall velocity and wall shear stress in a turbulent boundary layer*, Exp Fluids 45 (2008), pp. 1023–1035.
[37] A.N. Kolmogorov, *Dissipation of energy in a locally isotropic turbulence*, Doklady Akad. Nauk SSSR 32 (1941).
[38] L. Jie, *Etude detaillée des structures coherentes de la zone tampon de la turbulence de paroi a l'aide de données de PIV stereoscopique*, Ecole Centrale de Lille et Université de Lille, 2006.